


Phase engineering of relaxor ferroelectricity in van der Waals crystal

Received: 5 September 2025

Accepted: 28 January 2026

Published online: 09 February 2026

 Check for updates

Tao Yang^{1,2,4}, Yinchang Ma^{1,4}, Dongxing Zheng¹, Weili Deng², Chen Liu¹, Maolin Chen¹, Kairan Mai¹, Xiang Lv³, Xiaowen Zhang¹, Jingkai Xu¹, Baoyu Wang¹, Yan Li¹, Meng Tang¹, Guo Tian², Weiqing Yang² & Xixiang Zhang¹✉

Phase engineering of two-dimensional van der Waals materials offer a rich landscape to uncover the potential ferroelectric properties. The precisely controlling phases in these reduced dimensional materials with the unique atomic arrangement are crucial. Herein, through a novel phase engineering approach, we synthesize $\text{CuInP}_2(\text{S}_{1-x}\text{Se}_x)_6$ crystal with controllable coexistence of monoclinic and trigonal phases, and experimentally realize relaxor ferroelectricity in low-dimensional materials. Composition tailoring creates an intermediate phase transition region, which facilitates the evolution of ferroelectricity into relaxor ferroelectricity and eventually superparaelectricity. The relaxor ferroelectric properties are verified by the hysteresis-free polarization switching and diffused phase transition. High-resolution transmission electron microscopy reveals that edge dislocations play a critical role in forming locally disordered polar structures. When integrated it into a memristor device, the relaxor crystal with nanodomains demonstrates an increased number of analog resistance states and lower operating voltages compared to conventional ferroelectric crystals. This work establishes a phase engineering strategy to tailor ferroelectric behavior in low-dimensional materials, offering substantial potential for future electronic applications.

Significant research has been focused on polarization switching in ordered ferroelectric materials, which plays a key role in advanced electronic devices, such as ferroelectric field-effect transistors, ferroelectric tunnel junctions, and ferroelectric memristors^{1–3}. The urgent demand for high-density integration and ultralow-power consumption has prompted the exploration of ferroelectric thin film at atomic thickness limit^{4,5}. However, sustaining ferroelectric order at reduced thickness remains a critical challenge, as it is severely perturbed by delicate energy balance that is driven by boundary conditions and depolarization field^{6,7}. Although ferroelectrics have been achieved in thin films via epitaxial growth on lattice-matched substrates, the

dependence on such substrates constrains integration into electronic devices, and thus limits potential practical applications^{8,9}. In contrast, two-dimensional (2D) van der Waals (vdW) ferroelectric materials, featured by the absence of dangling bonds and remain the ferroelectricity down to monolayer thickness, offer a transformative platform for next-generation miniaturized electronic devices^{10–12}.

Controlling the phase in 2D vdW materials allows probing exotic physical phenomena in condensed matter physics, particularly enabling the full exploitation of 2D ferroelectrics at the atomic thickness^{13–15}. Considerable research has been focused on phase engineering for creating 2D heterostructures, superlattices and moiré

¹Physical Science and Engineering Division, King Abdullah University of Science and Technology (KAUST), Thuwal, Saudi Arabia. ²Key Laboratory of Advanced Technologies of Materials (Ministry of Education), School of Materials Science and Engineering, Southwest Jiaotong University, Chengdu, China. ³College of Materials Science and Engineering, Sichuan University, Chengdu, China. ⁴These authors contributed equally: Tao Yang, Yinchang Ma.

✉ e-mail: xixiang.zhang@kaust.edu.sa

systems through straightforward mechanical exfoliation and restacking, that reveals distinct physical properties and exceptional performance^{16,17}. While this approach has led to ground-breaking discoveries in sliding ferroelectrics, topological polar textures and superconductivity, the scalability and practicality of the assembled heterostructures remain significant limitations for technological implementation^{18,19}. Capturing the full potential of 2D materials requires robust and scalable synthesis of these atomical scale thickness materials and their heterostructures with designable spatial modulation of chemical compositions and electronic structures. The extreme aspect ratio, lack of intrinsic substrate and the atomically thin nature render them highly susceptible to defects and external perturbations (electronic, optical and mechanical)^{20,21}. Thus, precise and efficient phase engineering is a critical challenge for unlocking the transformative potential of low dimensional materials.

Analogous to non-stoichiometric phase engineering in conventional oxides, the multiple phases in 2D materials can be finely synthesized by tailoring the composition ratio^{22,23}. Here, we demonstrate a mixed-phase 2D system exhibiting a ferroelectric phase transition by controlling the ratio between monoclinic and trigonal phases that coexist in $\text{CuInP}_2(\text{S}_{1-x}\text{Se}_x)_6$ crystals. The phase control could induce superlattice modulations and local heterogeneous polar structures, facilitating the transition from ferroelectric (FE) to relaxor ferroelectric (RFE), superparaelectric (SPE), or paraelectric (PE), which is manifested by flatten free energy profile. The synthesis and composition of $\text{CuInP}_2(\text{S}_{1-x}\text{Se}_x)_6$ was characterized using energy dispersive X-ray spectroscopy (EDS), electron probe microanalyzer (EPMA), Raman spectroscopy. The local heterogeneous polar structure was investigated by X-ray diffraction (XRD), high-angle annular dark-field scanning transmission electron microscopy (HAADF-STEM), selected area electron diffraction (SAED), and second harmonic generation (SHG). Temperature-dependent ferroelectric and dielectric measurements confirmed the relaxor behavior through a hysteresis-free polarization response and frequency dispersion of dielectric permittivity. Additionally, the evolution of domain size and coercive voltage was investigated using piezoresponse force microscopy (PFM). Finally, the integration of 2D relaxor crystals into memristor devices exhibit enhanced analog resistance states and low operation voltages, demonstrating the potential for advanced electronic applications.

Results

Strategy for phase-engineering

The introduction of external elements into crystals has been an effective strategy for tuning structural phase transitions and material properties. In 2D layered transition-metal thio- and seleno-phosphates, CuInP_2S_6 crystallizes in ferroelectric monoclinic phase (space group Cc), whereas the $\text{CuInP}_2\text{Se}_6$ adopts a distinct ferroelectric trigonal phase (space group $P31c$)^{24,25}. Inspired by this structural diversity, we hypothesized that partial substitution of S with Se in $\text{CuInP}_2(\text{S}_{1-x}\text{Se}_x)_6$ crystal framework could lead to a controlled coexistence of these distinct phases and phase boundaries. Such phase coexistence results in local heterogeneous structure and polar nanoregions, which are expected to give rise to novel ferroelectric behaviors^{26,27} (Fig. 1a).

To systematically explore the evolution of structure and ferroelectric properties, we synthesized a series of $\text{CuInP}_2(\text{S}_{1-x}\text{Se}_x)_6$ crystals using the chemical vapor transport (CVT) method (details are presented in the Experimental Section). The Se substitution is confirmed by EDS and Raman analyses, and the accurately Se content of 0%, 0.8%, 2.6%, 4.2% and 6.9% are obtained using EPMA (Supplementary Note 1, Supplementary Fig. 1 and Supplementary Table 1). Given that Se has a larger ionic radius and lower electronegativity compared to S, the substitution introduces both structural and electronic perturbations to the lattice, weakening electrostatic constraints of Cu^{1+} cation and consequently altering the hopping motion of ions and structural stability of crystals^{25,28}. As Se content increased from 0% to 6.9%, the

gradually increased vibration peak at 346 cm^{-1} in Raman spectroscopy demonstrate the emergence of $[\text{P}_2(\text{S}_{1-x}\text{Se}_x)_6]^{4-}$ anion (Fig. 1b). In contrast, the intensities of the Cu^{1+} vibration peak at 315 cm^{-1} is reduced with higher Se content, indicating that the mixed S-Se chalcogen environment disrupted the hopping motion of the Cu^{1+} cations. And the simultaneous broadening of the both 315 cm^{-1} and 346 cm^{-1} peaks demonstrates that Se substitution enhance lattice instability, which drives the formation of heterogeneous structures. These compositional modifications significantly influence ferroelectric behavior, which is revealed in phase diagrams derived from the temperature-dependent ferroelectric and dielectric permittivity analysis (Fig. 1c, Supplementary Note 2 and Supplementary Figs. 2 and 3). As the Se content increases, the ferroelectric transition from FE to RFE and subsequently to SPE phase was observed at room temperature, and the T_m (where the dielectric permittivity reaches its maximum) undergoes a significant shift toward low temperature. At low temperatures, the FE converts to antiferroelectric (AFE) phase only. Notably, these phase transitions occur at the Se content of 2.6%, which suggests that the phase coexistence is established at this composition.

Local heterogeneous polar structure

To elucidate the mechanism underlying these phase transition, the microstructure of the crystal was performed using XRD and SAED. The clear diffractions peaks at 13.4° , 27.1° , 41.3° and 56.3° corresponding to the (002), (004), (006) and (008) planes, respectively, which indicate the 2D crystal stacks along the c -axis (Fig. 2a). Notably, for $x = 2.6\%$, the local substitution of Se induced gradient strain leads to grain size refinement, interlayer dislocations, and amorphous phases, causing the broadening of the (002) diffraction peak²⁹. As the Se content surpass 2.6%, the more uniform distribution of Se effectively releasing the accumulated strain and improving the local stacking order, resulting in the recovery of sharper (002) diffraction peak. And the diffraction peaks shift to larger angles, reflecting a reduction in interlayer distance along the c -axis. Additionally, the gradual decrease in intensity of the (004), (006) and (008) peaks with increasing Se content is related to local heterogeneous structure. These structures modifications might result in the emergence of trigonal phase with small interlayer distance, where the S atoms shift towards to the layer gap, and Cu atom move towards to the inner layer induced by steric hindrance effects. Furthermore, based on SAED patterns along the (001) axis, the typical diffraction spots of monoclinic structure were identified at $x = 0\%$, consistent with prior reports^{30,31} (Fig. 2b). For $x = 2.6\%$, the superlattice diffraction spots corresponding to the monoclinic phase diffraction, along with weak trigonal phase diffraction spots demonstrate the phase coexistence structure. The corresponding atomic-scale structural evolution can be directly observed in the HAADF-STEM images along the (001) direction (Supplementary Fig. 5). The superlattice structure was confirmed through the satellite peaks in the reciprocal lattice at bc plane for $x = 2.6\%$, which was investigated by single-crystal X-ray diffraction³² (Supplementary Fig. 6). These results indicate that the integration of trigonal and monoclinic phases forms a superlattice structure within the 2D crystal, leading to a locally heterogeneous polar structure.

Furthermore, the HAADF-STEM was conducted to uncover the atomic-scale microstructure of the coexisting multiphase. During the CVT growth, the Se atoms incorporate into the lattice under near-equilibrium conditions, leading to macroscopically homogeneously distribution at S sites. The monoclinic and trigonal phases can be determined by the angles between a - and c -axis and the interlayer distance along the (010) plane (Supplementary Note 4 and Supplementary Fig. 7). For Se content below 2.6%, the substituting Se atoms are randomly and sparsely distributed within the 2D layers, and the induced point defects are insufficient to distort the lattice, maintaining a homogeneous single-phase structure. And the independent monoclinic phase was observed, characterized by the angle of 98.9° between

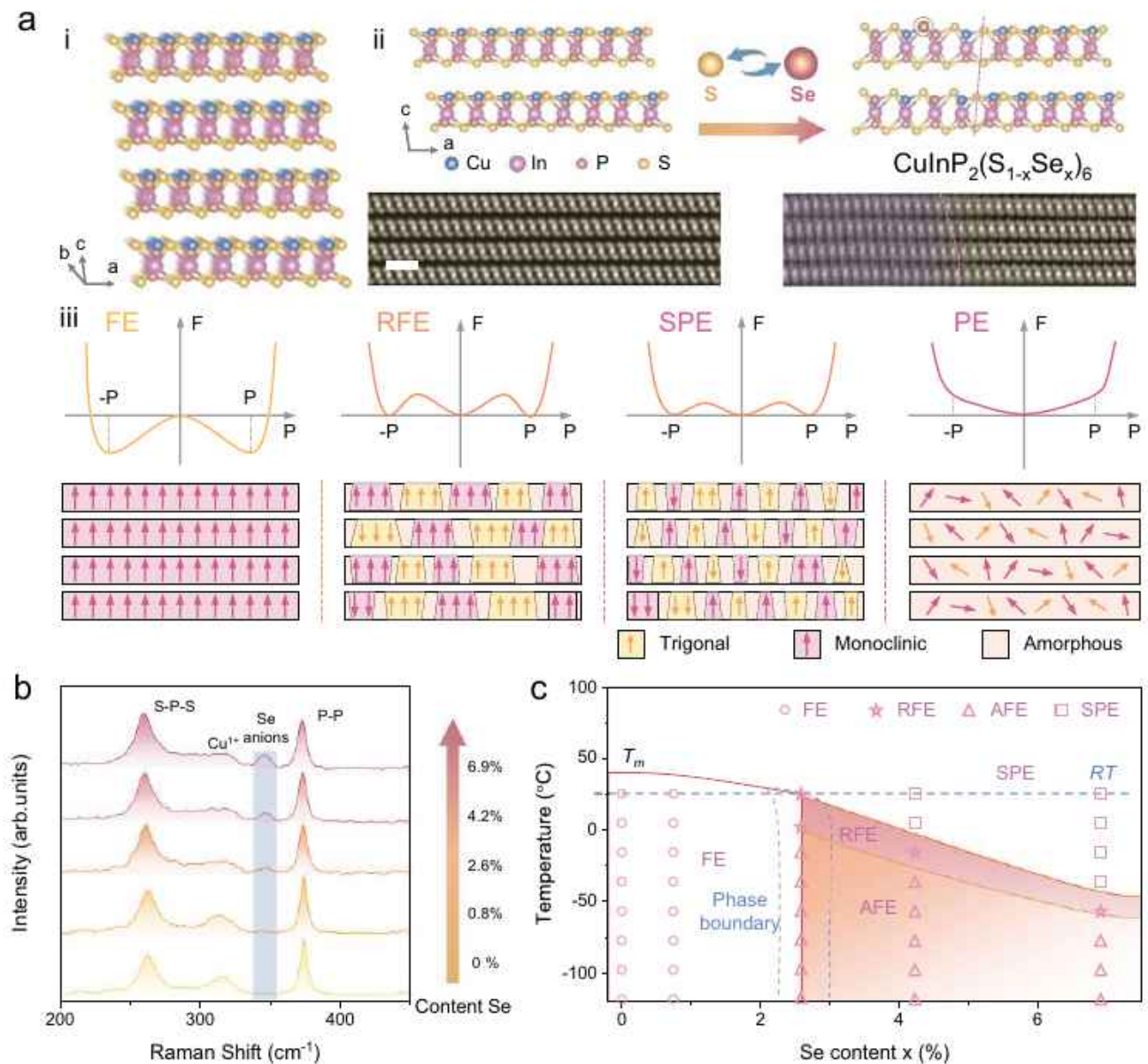


Fig. 1 | Design and control of phase engineering to achieve the relaxor ferroelectric. a Coexisting phase of monoclinic and trigonal to control the ferroelectric behavior. (i) The crystal structure of the 2D $\text{CuInP}_2(\text{S}_{1-x}\text{Se}_x)_6$ along the c -axis. (ii) Substitution of S with Se induced the coexisting phase in $\text{CuInP}_2(\text{S}_{1-x}\text{Se}_x)_6$ crystals, as the observed phase coexistence in the TEM image of the layered crystal along the cross-section, scale bar, 1 nm. (iii) The schematic diagram of gradually disordered polar structure for the phase transition from ferroelectric to paraelectric corresponding

to Landau energy. **b** Raman spectra of the mixed-phase $\text{CuInP}_2(\text{S}_{1-x}\text{Se}_x)_6$ crystal with introduced Se. **c** Phase diagram of the mixed-phase crystal with respect to Se content and temperature, where symbols mark tested samples with various compositions. The temperature of maximum dielectric permittivity (T_m) is extracted from the temperature-dependent dielectric spectra at 10 kHz. The abbreviations represent ferroelectric (FE), relaxor ferroelectric (RFE), superparaelectric (SPE) and antiferroelectric (AFE), with room temperature (RT) indicating room temperature.

the a and c axis and clearly vdW gap (Supplementary Figs. 5 and 8). With the Se content increase to 2.6%, local Se enrichment near defect sites induces sufficient strain to distort the lattice, leading to the formation of dislocation and trigonal phase. These localized strain fields further induce interlayer sliding within the layered crystal structure, leading to the coexistence of monoclinic and trigonal phases, as clearly observed in Fig. 2c. Edge dislocation regions, marked by orange dashed lines, indicated that substitution of S by Se, with its larger atomic radius, produced lattice stress by steric hindrance effects as illustrated in the lower right section of Fig. 2c. This can be further corroborated by the presence of dislocation cores identified through the geometric phase analysis (GPA) featured by pronounced shear stress (ϵ_{xy}) concentration. The strain gradient facilitated the formation of trigonal phase under compressive strain between the dislocation

and monoclinic phase, resulting in nearly 90° angle between the a and c axis in unit cell. Multiphase structure that comprises dislocation regions (~ 5 nm), trigonal phase regions (~ 20 nm), and residual monoclinic phases, formed disordered polar regions (Supplementary Fig. 8), which provides detailed insights into the local polar nanoregions in the multiphase coexistence structure.

The SHG signal is a sensitive probe for detecting the local symmetry breaking in materials, with the intensity (I) is proportional to the square of the polarization (P^2). For $x=0\%$, the uniform monoclinic phase exhibit strong SHG signals due to pronounced asymmetry and large polarization ordering (Supplementary Fig. 9). As the Se content increases, the emergence of the trigonal phase disrupts polarization ordering and reduces asymmetry, which leads to the gradual decline of SHG intensity. The angle-dependent SHG measurements reveal similar

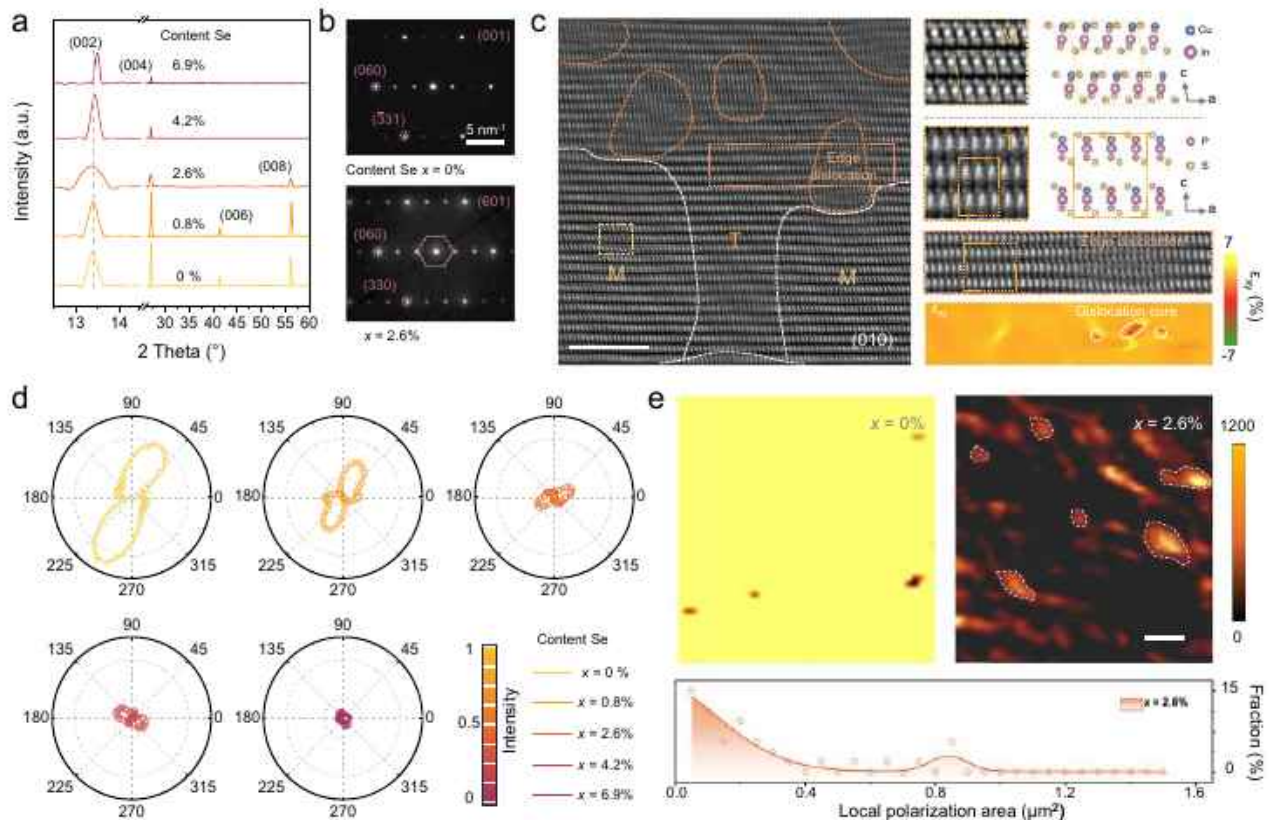


Fig. 2 | Local heterogeneous polar structure at the phase coexistence structure. **a** XRD spectra of mixed-phase crystal with Se content increasing from 0% to 6.9%. **b** SAED patterns along the (001) axis for Se content at 0% and 2.6%. **c** Cross-sectional HAADF-STEM image of the layered crystal at Se content of 2.6% showing the monoclinic (M), trigonal (T) phase and edge dislocation, scale bar, 5 nm. The edge dislocation region is marked with orange dashed lines. The diffraction

patterns show monoclinic and trigonal phases. Geometric phase analysis (GPA) was applied to extract the strain distribution at the edge dislocation regions. **d** Polarization angle-dependent SHG spectra of the mixed-phase crystal with Se content increase from 0% to 6.9%. **e** SHG mapping of Se content at 0% and 2.6% with a selected region of $10 \mu\text{m} \times 10 \mu\text{m}$, scale bar, $1 \mu\text{m}$. The bottom is the quantitative analysis of polar area distribution.

sixfold rotation symmetry patterns across samples, even for the weakest intensity crystal at $x = 6.9\%$, indicating the persistence of polarization in the heterogeneous polar structure (Fig. 2d). Besides, the SHG mapping exhibits uniform polarization regions for $x = 0\%$, while the small and weak polarization region was observed at the $x = 2.6\%$, corresponding to the coexisted phases with local heterogeneous structure (Fig. 2e). The detailed analysis of polarization region areas shows that most polar regions for $x = 2.6\%$ are concentrated around $0.2 \mu\text{m}^2$. These results confirm that the coexisting multiphases induce local heterogeneous structure, which decreases polar anisotropy and forms polar nanoregions.

Relaxor ferroelectric property

The coexisted multiphase with local heterogeneous polar structure is closely associated with the ferroelectric behavior. The polarization-electric field (P - E) loops and corresponding current-electric field (I - E) curves of the mixed-phase crystals $\text{CuInP}_2(\text{S}_{1-x}\text{Se}_x)_6$ were measured at room temperature (Supplementary Note 5 and Supplementary Fig. 10). To avoid leakage current influence, the P - E loops was carried out at frequency 800 Hz (Fig. 3a). At $x = 0\%$, the sample exhibits typical ferroelectric feature with large maximum polarization (P_m) of $4.4 \mu\text{C cm}^{-2}$ and visible remanent polarization (P_r) of $3.0 \mu\text{C cm}^{-2}$, which leading to clearly hysteresis loops. As the Se content increases to $x = 2.6\%$, the P_r dropped sharply to $1.2 \mu\text{C cm}^{-2}$, while the P_m remains relatively stable at $3.7 \mu\text{C cm}^{-2}$. The reduced hysteresis loops indicate transition from FE to RFE state. With further increases in Se to 6.9%, both P_r and P_m decreased to 0.2 and $1.0 \mu\text{C cm}^{-2}$, respectively, which displays slim and

nearly linear hysteresis loops characteristic of the SPE-like state. The similar polarization evolution of P_r and P_m is also observed in the exfoliated few-layer crystals, confirming that the relaxor ferroelectric behavior can be preserved in this two-dimensional crystal (Supplementary Fig. 11). Notably, the crystal of $\text{CuInP}_2(\text{S}_{1-x}\text{Se}_x)_6$ possesses a ferroelectric configuration, which the Cu and In ions exhibit antiparallel displacements with unequal magnitudes, resulting in a non-zero net polarization³³. Since the contribution of In ion to the polarization is negligible, the ferroelectric behavior is fundamentally governed by the displacement and positioning of Cu ions, which can occupy three types of position^{31,34}: off-center position (Cu1), center position (Cu2); and the interlayer space (Cu3) (Fig. 3b). In the monoclinic phase, Cu ions at S plane predominantly occupy the off-center Cu1 site, which leads to a significant polarization due to large ionic displacement. Conversely, in the trigonal phase, Cu ions preferentially migrate towards the more centered Cu2 intralayer position, resulting in weaker polarization due to a much small displacement. Density functional theory (DFT) calculations also confirmed that the trigonal phase ($\text{CuInP}_2\text{Se}_6$) has weaker polarization compared to the monoclinic phase (CuInP_2S_6) (Fig. 3c). Moreover, the trigonal phase was found to have lower energy barriers, which facilitates polarization reversal (Fig. 3d). These results collectively confirm the FE-RFE-SPE transitions in the mixed-phase crystal with the increase of Se content.

Another feature of relaxor ferroelectric is the presence of a diffused phase transition and frequency dispersion around the temperature-dependent dielectric peaks (T_m). To characterize these properties, the dielectric permittivity of mixed-phase $\text{CuInP}_2(\text{S}_{1-x}\text{Se}_x)_6$

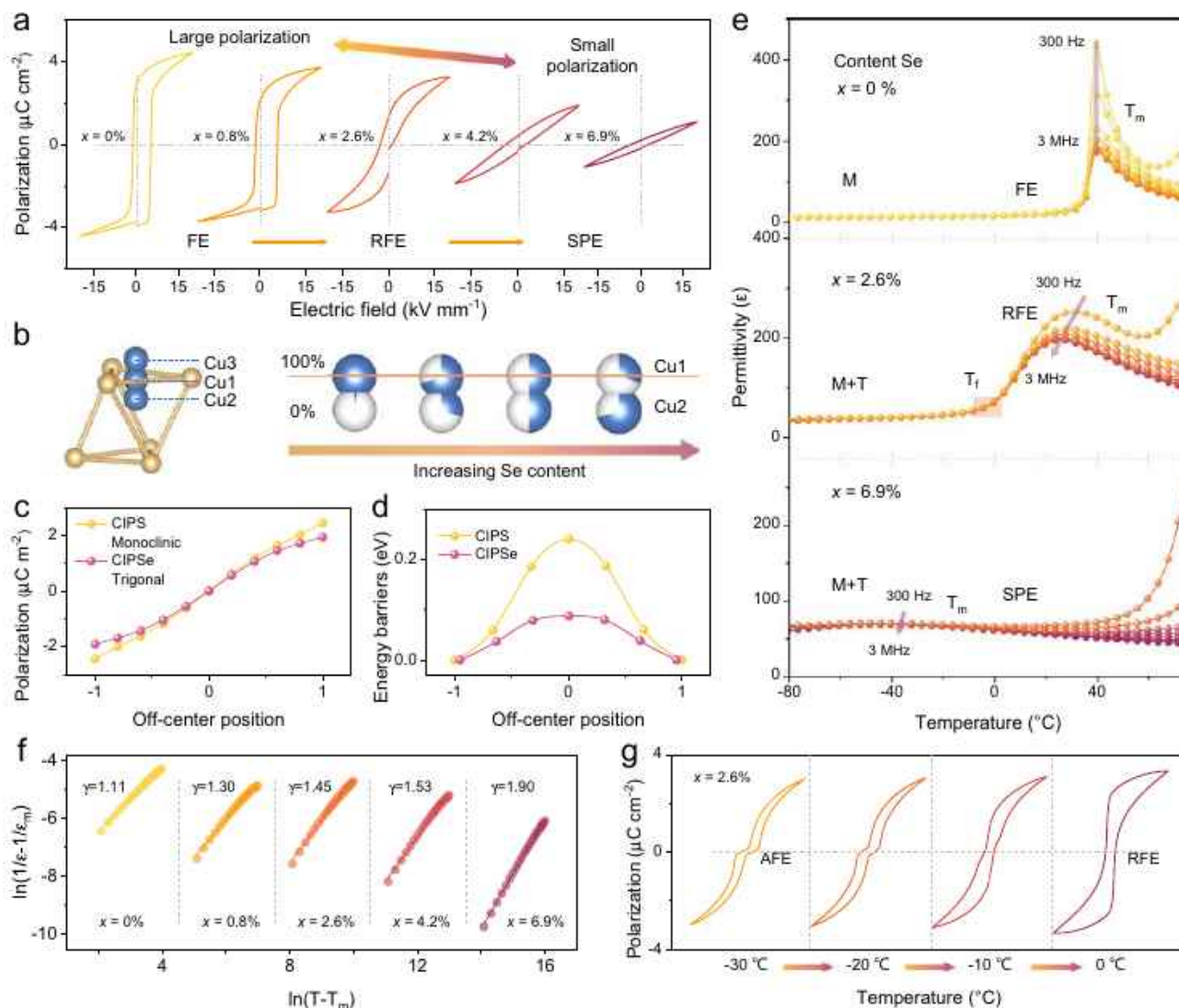


Fig. 3 | Polarization and dielectric behavior variation during the phase transition from ferroelectric to superparaelectric. **a** P - E loops at the electric field of 20 kV mm^{-1} and 800 Hz with the Se content varying from 0% to 6.9% . **b** Three possible Cu ion occupation states in a sulfur octahedral frame. The Cu ions gradually move toward interlayer Cu2 sites with the Se content increase, which forms the trigonal phase. **c**, **d** DFT-calculated polarization and reversal energy barriers for

the monoclinic and trigonal phase. The off-center position of 1 and -1 corresponds to polarization at up and down for the Cu ion. **e** Temperature-dependent of dielectric permittivity from -80 to 75 °C for the Se content of 0% , 2.6% and 6.9% . **f** Fitting relaxor diffuseness factor of temperature-dependent dielectric at 10 kHz . **g** Phase transition from AFE to RFE at freezing temperature (T_f) with Se content of 2.6% .

crystal was measured across a temperature range of -150 °C to 100 °C and frequency range of 300 Hz to 3 MHz (Supplementary Note 3 and Supplementary Fig. 3). In contrast to the sharp dielectric peaks for $x = 0\%$ with typical ferroelectric phase, the gradual shift of phase transition temperature at relatively small range with frequency confirms the relaxor-like ferroelectric at composition $x = 2.6\%$ and 6.9% (Fig. 3e). The degree of dispersion was quantified using the relaxor diffuseness factor (γ) derived from modified Curie-Weiss law^{35,36}: $\frac{1}{\epsilon} - \frac{1}{\epsilon_m} = \frac{(T - T_m)^\gamma}{C}$, where the ϵ_m is the maximum dielectric constant at T_m , and C is the Curie-like constant, where the $\gamma = 1$ corresponds to a typical ferroelectric behavior and $\gamma = 2$ represents an ideal relaxor ferroelectric. The γ values increase progressively from 1.11 for $x = 0\%$ to 1.45 for $x = 2.6\%$, and 1.9 for $x = 6.9\%$, demonstrating the enhanced relaxor property (Fig. 3f). And the γ of 1.45 at $x = 2.6\%$ indicates the initial transition from FE toward RFE, which corresponding to the emergence of phase coexistence structure. Notably, for $x = 2.6\%$, an abnormal behavior of the dielectric peak T_m shifts towards lower temperatures as frequency increases was observed, which attributed

to the ionic conduction effects previously reported in relaxor ferroelectric materials^{29,37} (Supplementary Note 3 and Supplementary Fig. 4a). Besides, the gradual decrease of phase transition temperature T_m was observed as the Se content increases, which could be attributed to the local heterogeneous structure and lattice instability. At $x = 2.6\%$, the T_m is observed at 25 °C, close to room temperature (Supplementary Fig. 9b). Consequently, the maximum dielectric permittivity was observed at $x = 2.6\%$, with the subsequent decrease of dielectric permittivity for the x exceeding 2.6% at room temperature (Supplementary Fig. 9c). Moreover, the thermal stability of dielectric permittivity was substantially improved with the greater Se content. For the $x = 6.9\%$, the highly stabilized permittivity of approximately 60 was maintained across a wide temperature range from -100 °C to 50 °C, in contrast to $x = 0\%$, where stability was limited to a narrower range (-100 °C to 20 °C) with a permittivity of 14 . This enhancement is attributed to the pronounced relaxor behavior, which enables the polarization to gradually vanish even above the T_m . And the increase of dielectric permittivity is associated with the local polar regions, which

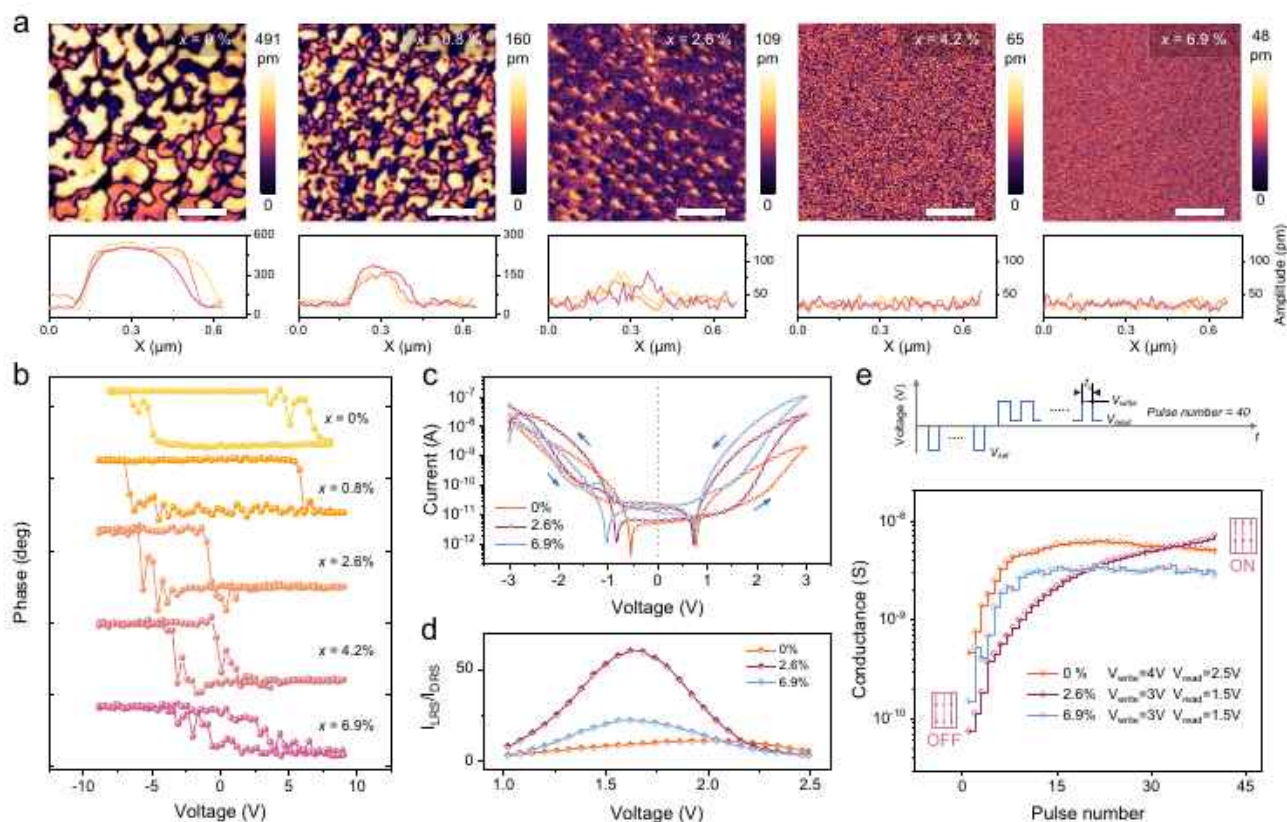


Fig. 4 | Domain structure and electric property variation with relaxor ferroelectric. **a** PFM amplitude image of domain structure evolution with Se content increasing from 0% to 6.9%, scale bar, 1 μm . Amplitude profile along several domains shows the domain evolution. The PFM measurement was performed at room temperature and the sample are not polarized. **b** PFM phase hysteresis loops with Se content increasing from 0% to 6.9% at voltage sweep from -9 to 9 V and

1 Hz. **c** I - V sweeping curves from -3 to 3 V for Se content of 0%, 2.6% and 6.9%. **d** Switching ratio (I_{LRS}/I_{HRS}) dependence on the voltage. The current was extracted from the I - V curves at voltages from 1 to 2.5 V. **e** Polarization switching from down-to-up with consecutive positive pulse voltage, mimicking the long-term potentiation behavior of artificial synapses.

allows larger polarization response at lower electric field. Additionally, as the temperature approached the relaxor freezing temperature (T_f), a phase transition from AFE to RFE was observed, as depicted in Fig. 3g and Supplementary Fig. 12, further corroborating the phase evolution shown in Fig. 1c. These results demonstrate the appearance of relaxor ferroelectric at the phase boundary with monoclinic and trigonal phase.

Electrical properties

The appearance of local heterogeneous polar structure typically causes the domains size refinement within the phase coexistence. As validated by PFM, the clear reduce of the domain size is observed in few-layer crystals as the Se content increase (Fig. 4a, Supplementary Note 6 and Supplementary Figs. 13 and 14), with domains nearly disappear at the $x = 4.2\%$ and 6.9% . This further demonstrate that the relaxor ferroelectric behavior could be remained in the low dimensional crystal. According to the Landau phenomenological theory, the competition between the refined domains energy and interfacial energy lowers the energy barrier for polar rotation, and makes the flatten free energy profile²⁷. This was further corroborated by PFM phase hysteresis loop, which showed decreasing switching voltages for domain reversal with increasing Se content (Fig. 4b). Therefore, the formation of nanodomains in relaxor ferroelectric enables multiple resistance state modulation under lower operating voltages, making it well-suited for the memristor devices rely on repeated write-read operations. To further investigate the resistance behavior during the domain-switching process, the crystal was exfoliated and integrated into two-terminal memristor device with a vertical structure (Au/Ti/

CuInP₂(S_{1-x}Se_x)₆/Au), which could mimic artificial synaptic functions (Supplementary Note 7). From the sweeping voltage from -3 to 3 V at a 0.03 V step, the clear hysteretic current-voltage (I - V) curves were observed between the high resistance state (HRS) and low resistance state (LRS) for 0%, 2.6% and 6.9% (Fig. 4c and Supplementary Fig. 15). The maximized switching ratio (I_{LRS}/I_{HRS}) was achieved at write voltage of 1.62 V for $x = 2.6\%$, due to the heterogeneous polar structure enhanced polarization rotation in the relaxor ferroelectric structure (Fig. 4d). Furthermore, the resistance switching dynamics, linked to polarization rotation, was analyzed using pulse sequences voltage (Supplementary Fig. 16). The upward and downward polarization were defined as ON and OFF resistance state, respectively. The device was first set to the OFF state by pulse voltage $V_{\text{set}} = -3$ V (duration $t_d = 50$ ms), followed by the application of pulse voltages V_{write} and V_{read} . Over the 40 consecutive pulses, the resistance exhibited step-wise increases, mimicking the long-term potentiation (LTP) behavior of artificial synapses (Fig. 4e). Notably, the multi-state resistance of RFE at 2.6% keeps increasing depending on the pulse number, while the FE and SPE with $x = 0\%$ and 6.9% reaches saturation rapidly after a few pulses. This indicated the RFE exhibits many analog resistance switching states in the memristor, which can be ascribed to multiple polarization states as nanodomains gradually switching. Additionally, these refined nanodomains effectively reduce the coercive field in RFE crystals, making low operation voltages for memristor device. At $x = 2.6\%$ and $x = 6.9\%$, the required lowest $V_{\text{write}} = 3$ V and $V_{\text{read}} = 1.5$ V were lower than $x = 0\%$ with $V_{\text{write}} = 4$ V and $V_{\text{read}} = 2.5$ V. These low operation voltages making relaxor ferroelectric crystal candidates for highly energy-efficient memristor applications.

Discussion

In this work, the phase-engineering at $\text{CuInP}_2(\text{S}_{1-x}\text{Se}_x)_6$ layered crystal was achieved by non-stoichiometric method. The phase coexistence of monoclinic and trigonal phase in 2D materials could be controlled by regulating the chemical composition during the growth. The phase competition in mixed-phase crystal induces superlattice and local heterogeneous polar structure. Furthermore, this phase competition reveals a sequential transformation of ferroelectricity, evolving from FE to RFE and SPE phases at room temperature, with a notable transition to AFE behavior at low temperatures. The RFE phase with polar nanoregions and low coercion voltage significantly enhancing the memristor performance, making it a promising candidate for energy-efficient, high-density memory applications. These findings represent a significant breakthrough in overcoming the dimensional limitations of relaxor ferroelectrics through phase engineering, and provide a robust framework for designing advanced two-dimensional materials with superior performance for next-generation electronic devices.

Methods

Growth of 2D crystal

The single crystal of $\text{CuInP}_2(\text{S}_{1-x}\text{Se}_x)_6$ were growth by the chemical CVT method with iodine as the transport agent¹⁸. High pure precursor materials, including Cu (99.99%, Sigma-Aldrich), In (99.99%, Sigma-Aldrich), P (99.999%, Sigma-Aldrich), S (99.98%, Alfa Aesar) and Se (99.99%, Sigma-Aldrich) were mixed in quartz tube with a nominal stoichiometric proportion of 1:1:2:6:0, 1:1:2:5.982:0.018, 1:1:2:5.916:0.084, 1:1:2:5.85:0.15, 1:1:2:5.748:0.252, corresponding to the Se content 0%, 1%, 3%, 5% and 8%, respectively. This slightly deviation is ascribed to the variations in vapor transport efficiency and minor weighing inaccuracies of the elemental precursors during the CVT growth process. Then they were sealed under a vacuum of 10^{-4} mbar through the high-temperature torch. The crystals were growth in a dual-temperature zone tubular furnace, with source zone maintained at 750 °C and the growth zone at 700 °C, over a period of 7 days. The gradually heating and cooling temperature rate of 2°C min^{-1} was maintained throughout the process. Upon completion of the growth, plate-like crystals with lateral dimensions of several millimeters and thicknesses of several micrometers were obtained in the crystallization zone.

Structure characterization

Detailed crystal structure analysis was conducted using Single-crystal X-ray diffraction with Bruker D8 Venture diffractometer to determine the crystal structure, with data processing, cell refinement, and calculations conducted via APEX4, SAINT, and SADABS software. And the crystals were mounted on silicon during XRD measurements. Elements concentration was characterized using a scanning electron microscope (Nova SEM) equipped with an EDS and EPMA (JEOL JXA-iHP200F). Raman spectroscopy was acquired using a WITec alpha300 apyron confocal system with a 532 nm excitation laser. Cross-section TEM lamellae were prepared using a Thermo Fisher Helios G4 system. Atomic-scale conformations were captured with HAADF-STEM using an FEI Titan ST transmission electron microscope.

SHG measurement

Polarization-dependent SHG measurements and SHG mapping were conducted using a WITec alpha300 Raman system. A 1064 nm excitation laser beam was focused on the objective focal plane, with its polarization controlled by a half-wave plate. Angle-dependent SHG measurements were performed in 2° increments using a motorized rotational stage, and the SHG intensity at each angle was averaged over three counts with an integration time of 0.5 seconds per step. For SHG mapping, a selected region of $10\ \mu\text{m} \times 10\ \mu\text{m}$ was scanned under consistent incident light intensity, with a scan rate of 50 ms per pixel.

PFM measurement

Ferroelectric domain characterization was conducted using piezo-response force microscopy (PFM) on an Asylum Research MFP-3D system, operating in dual AC resonance tracking mode (DART-PFM) at room temperature. Conductive Pt-coated Si tips with a spring constant of $3\ \text{N m}^{-1}$ and a resonance frequency of 75 kHz were used for the measurements. Domain imaging was performed with an AC voltage of 1 V applied at the tip, operating at a tip-sample contact resonance frequency of 315 kHz. The phase switching voltage was measured by applying the sweep voltage from -9 to 9 V with 1 Hz and drive voltage of 1 V at the tips, the phase curves can be obtained at the off state.

Device fabrication and measurement

The 2D crystal flakes were obtained by mechanically exfoliating them from the bulk crystal and were identified as high-quality using optical microscopy. The patterned bottom electrode was fabricated by depositing 10 nm Ti and 30 nm Au onto a SiO_2/Si substrate using a laser writer (DWL66+) and e-beam evaporation. The exfoliated 2D crystal flakes were then transferred onto the bottom electrode using the dry transfer method with a polymer stamp. The top electrode was defined using a laser writer, followed by deposition of 10 nm Ti and 80 nm Au through e-beam evaporation. Electrical measurements of the device were performed using a Keithley 4200 semiconductor characterization system at room temperature in an ambient environment.

Ferroelectric and dielectric measurement

Before the measurement carried out, the circle Au electrode (diameter 1 mm) was deposited on both sides of the crystal at thickness of 100 nm. The ferroelectric property was investigated by the ferroelectric analyzer with a Sawyer-Tower circuit (axiACCT, TF Analyzer 2000E). The P - E loops were performed by the bipolar electric fields of the triangular wave in DHM mode, and the frequency from 100 Hz to 1 kHz. The temperature dependent P - E loops were obtained from -120 to 10°C at increase step of 10°C . The dielectric permittivity was acquired over a broad frequency using the Alpha-A High Performance Frequency Analyzer by applying an AC voltage of 0.1 V. With the temperature increase from -150 to 100°C , the dielectric spectroscopy from 300 Hz to 3 MHz was measured at the temperature increase step of 2°C .

DFT calculations

First-principles calculations were performed using the Vienna Ab initio Simulation Package (VASP) with the projector-augmented wave (PAW) method and the Perdew-Burke-Ernzerhof (PBE) exchange-correlation functional^{39,40}. A plane-wave kinetic energy cut-off of 450 eV was chosen. For structural relaxations, a Gamma-centered k -points grid with $ka > 40\ \text{\AA}$ was used to sample the Brillouin zone, where k is the number of mesh points and a represents the lattice constants. A similar k -point mesh was used for all static runs. To prevent any spurious interaction between periodically repeated layers, a large vacuum space of at least $20\ \text{\AA}$ in the direction of c was applied. Structures were relaxed until the energy differences converged below 10^{-6} eV and forces within 1×10^{-2} eV/\text{\AA}. van der Waals corrections using the optB86b exchange-correlation functional were applied to precisely account for inter-layer interactions, particularly for materials like CuInP_2S_6 ^{41,42}. Solid-state nudged elastic band method (SSNEB) was employed to investigate the polarization reverse barrier⁴³. The spontaneous polarizations of the ferroelectric materials were computed using the Berry phase method, which incorporates contributions from both electronic and ionic parts⁴⁴.

Reporting summary

Further information on research design is available in the Nature Portfolio Reporting Summary linked to this article.

Data availability

All data generated in this study are provided in the paper or the Supplementary Information. Further data are available from the corresponding author upon request. Source data are provided with this paper.

References

- Chanthbouala, A. et al. A ferroelectric memristor. *Nat. Mater.* **11**, 860–864 (2012).
- Pan, X. et al. 2D materials for intelligent devices. *Sci. China Phys. Mech. Astron.* **66**, 117504 (2023).
- Wang, B. et al. Ultralow-pressure mechanical-motion switching of ferroelectric polarization. *Sci. Adv.* **11**, eadr5337 (2025).
- Yang, Q. et al. Ferroelectricity in layered bismuth oxide down to 1 nanometer. *Science* **379**, 1218–1224 (2023).
- Martin, L. W. & Rappe, A. M. Thin-film ferroelectric materials and their applications. *Nat. Rev. Mater.* **2**, 1–14 (2016).
- Gradauskaite, E. et al. Defeating depolarizing fields with artificial flux closure in ultrathin ferroelectrics. *Nat. Mater.* **22**, 1492–1498 (2023).
- Jiang, Y. et al. Enabling ultra-low-voltage switching in BaTiO₃. *Nat. Mater.* **21**, 779–785 (2022).
- Liu, H. et al. Giant piezoelectricity in oxide thin films with nanopillar structure. *Science* **369**, 292–297 (2020).
- Zeches, R. J. et al. A strain-driven morphotropic phase boundary in BiFeO₃. *Science* **326**, 977–980 (2009).
- Wang, C., You, L., Cobden, D. & Wang, J. Towards two-dimensional van der Waals ferroelectrics. *Nat. Mater.* **22**, 542–552 (2023).
- Ma, Y. et al. High-performance van der Waals antiferroelectric CuCrP₂S₆-based memristors. *Nat. Commun.* **14**, 7891 (2023).
- Lv, X., Zhu, J., Xiao, D., Zhang, X.-X. & Wu, J. Emerging new phase boundary in potassium sodium-niobate based ceramics. *Chem. Soc. Rev.* **49**, 671–707 (2020).
- Li, W., Qian, X. & Li, J. Phase transitions in 2D materials. *Nat. Rev. Mater.* **6**, 829–846 (2021).
- Zhang, J. et al. Interlayer reconstruction phase transition in van der Waals materials. *Nat. Mater.* **24**, 369–376 (2025).
- NG, A., HA, Z. & Njing, A. Phase landscapes in low-dimensional structures. *Nat. Mater.* **23**, 1301 (2024).
- Wang, L. et al. Bevel-edge epitaxy of ferroelectric rhombohedral boron nitride single crystal. *Nature* **629**, 74–79 (2024).
- Park, D. et al. Unconventional domain tessellations in moiré-of-moiré lattices. *Nature* **641**, 896–903 (2025).
- Pan, E. et al. Observation and manipulation of two-dimensional topological polar texture confined in Moiré interface. *Nat. Commun.* **16**, 3026 (2025).
- Naritsuka, M. et al. Superconductivity controlled by twist angle in monolayer NbSe₂ on graphene. *Nat. Phys.* **21**, 746–753 (2025).
- Hou, W. et al. Strain engineering of vertical molybdenum ditelluride phase-change memristors. *Nat. Electron.* **7**, 8–16 (2024).
- Liu, X. et al. On-device phase engineering. *Nat. Mater.* **23**, 1363–1369 (2024).
- Li, J. et al. Towards the scalable synthesis of two-dimensional heterostructures and superlattices beyond exfoliation and restacking. *Nat. Mater.* **23**, 1326–1338 (2024).
- Xue, F. et al. Observation of switchable polar skyrmion bubbles down to the atomic layers in van der Waals ferroelectric CuInP₂S₆. *Nat. Commun.* **16**, 2349 (2025).
- Vysochanskii, Y. et al. Phonon spectra and phase transitions in CuInP₂(Se_xS_{1-x})₆ ferroelectrics. *Ferroelectrics* **284**, 161–173 (2003).
- Beley, L. M. et al. Dipole glassy state evidence for CuInP₂(Se_xS_{1-x})₆ ferroelectric mixed crystals from Raman scattering and optical absorption data. *Ukr. J. Phys. Opt.* **8**, 13–24 (2007).
- Liu, Y. et al. Ferroelectric polymers exhibiting behaviour reminiscent of a morphotropic phase boundary. *Nature* **562**, 96–100 (2018).
- Pan, H. et al. Ultrahigh energy storage in superparaelectric relaxor ferroelectrics. *Science* **374**, 100–104 (2021).
- Yao, X. et al. Anomalous polarization enhancement in a van der Waals ferroelectric material under pressure. *Nat. Commun.* **14**, 4301 (2023).
- Shu, L. et al. Partitioning polar-slush strategy in relaxors leads to large energy-storage capability. *Science* **385**, 204–209 (2024).
- Deng, J. et al. Thickness-dependent in-plane polarization and structural phase transition in van der Waals ferroelectric CuInP₂S₆. *Small* **16**, 1904529 (2020).
- Li, T. et al. Realization of sextuple polarization states and interstate switching in antiferroelectric CuInP₂S₆. *Nat. Commun.* **15**, 2653 (2024).
- Zhou, X. et al. Lead-free ferroelectrics with giant unipolar strain for high-precision actuators. *Nat. Commun.* **15**, 6625 (2024).
- Morozovska, A. N. et al. Anomalous polarization reversal in strained thin films of CuInP₂S₆. *Phys. Rev. B* **108**, 054107 (2023).
- Brehm, J. A. et al. Tunable quadruple-well ferroelectric van der Waals crystals. *Nat. Mater.* **19**, 43–48 (2020).
- Li, R. et al. Giant dielectric tunability in ferroelectric ceramics with ultralow loss by ion substitution design. *Nat. Commun.* **15**, 3754 (2024).
- Yang, L. et al. Simultaneously achieving giant piezoelectricity and record coercive field enhancement in relaxor-based ferroelectric crystals. *Nat. Commun.* **13**, 2444 (2022).
- Liu, Y. et al. Chirality-induced relaxor properties in ferroelectric polymers. *Nat. Mater.* **19**, 1169–1174 (2020).
- Liu, C. et al. Magnetic Skyrmions above Room Temperature in a van der Waals Ferromagnet Fe₃GaTe₂. *Adv. Mater.* **36**, 2311022 (2024).
- Kresse, G. & Joubert, D. From ultrasoft pseudopotentials to the projector augmented-wave method. *Phys. Rev. B* **59**, 1758 (1999).
- Perdew, J. P., Burke, K. & Ernzerhof, M. Generalized gradient approximation made simple. *Phys. Rev. Lett.* **77**, 3865 (1996).
- Klimeš, J., Bowler, D. R. & Michaelides, A. Van der Waals density functionals applied to solids. *Phys. Rev. B* **83**, 195131 (2011).
- He, R. et al. Unconventional ferroelectric domain switching dynamics in CuInP₂S₆ from first principles. *Phys. Rev. B* **108**, 024305 (2023).
- Sheppard, D. et al. A generalized solid-state nudged elastic band method. *J. Chem. Phys.* **136**, 074103 (2012).
- King-Smith, R. & Vanderbilt, D. Theory of polarization of crystalline solids. *Phys. Rev. B* **47**, 1651 (1993).

Acknowledgements

This work has been supported by the “Semiconductor Initiative” and Office of Sponsored Research (OSR) of King Abdullah University of Science and Technology (KAUST) under award Nos. ORA-CRG10-2021-4665 and ORA-CRG11-2022-5031. This research was undertaken with the resources from the Supercomputing Core Laboratory at KAUST.

Author contributions

X.X.Z., T.Y., and Y.M. conceived and designed the work. Y.M., X.L., and T.Y. prepared the samples and carried out the temperature-dependent ferroelectric and dielectric measurements. Y.M. and M.T. collected the XRD and EDS data. J.X. and D.Z. conducted the single-crystal X-ray diffraction and processing data. X.W.Z. and Y.L. conducted the Raman and SHG tests. C.L. carried out the HAADF-STEM and SAED observation and analysis. Y.M. and T.Y. measured and analyzed the PFM. M.C., K.M., and B.W. fabricated the device and conducted I–V measurement. Y.M. and G.T. performed and analyzed the DFT calculations. W.D., Y.L., Y.M., and T.Y. analyzed the relaxor ferroelectric property. D.Z., W.Y., Y.M., and T.Y.

wrote the manuscript with input from all authors. X.X.Z. supervised this research.

Competing interests

The authors declare no competing interests.

Additional information

Supplementary information The online version contains supplementary material available at <https://doi.org/10.1038/s41467-026-69272-9>.

Correspondence and requests for materials should be addressed to Xixiang Zhang.

Peer review information *Nature Communications* thanks Anna Morozovska, Muhammad Sheeraz and the other anonymous reviewer(s) for their contribution to the peer review of this work. A peer review file is available.

Reprints and permissions information is available at <http://www.nature.com/reprints>.

Publisher's note Springer Nature remains neutral with regard to jurisdictional claims in published maps and institutional affiliations.

Open Access This article is licensed under a Creative Commons Attribution-NonCommercial-NoDerivatives 4.0 International License, which permits any non-commercial use, sharing, distribution and reproduction in any medium or format, as long as you give appropriate credit to the original author(s) and the source, provide a link to the Creative Commons licence, and indicate if you modified the licensed material. You do not have permission under this licence to share adapted material derived from this article or parts of it. The images or other third party material in this article are included in the article's Creative Commons licence, unless indicated otherwise in a credit line to the material. If material is not included in the article's Creative Commons licence and your intended use is not permitted by statutory regulation or exceeds the permitted use, you will need to obtain permission directly from the copyright holder. To view a copy of this licence, visit <http://creativecommons.org/licenses/by-nc-nd/4.0/>.

© The Author(s) 2026